Supporting Information

Supramolecular nanowires solely composed of cobalt and ruthenium salts enable enhanced stability and activity in light-driven hydrogen evolution

Eva Oswald[1], Giada Caniglia[1]*, Anna-Laurine Gaus[2], Martin Lämmle[3], Alexander K. Mengele[3], Sven Rau[3], Soumya Rajpal[1], Max von Delius[2], Giuseppe Ragusano[4], Marcus Rohnke[5], Tanveer Ahmed Shaik[6,7], Wei Wang[6,7], Volker Deckert[6,7], Robert Leiter[8], Johannes Biskupek[8], Ute Kaiser[8], Boris Mizaikoff[1], Christine Kranz[1]*

[1] Institute of Analytical and Bioanalytical Chemistry, Ulm University, Albert-Einstein-Allee 11, 89081 Ulm, Germany

[2] Institute of Organic Chemistry, Ulm University, Albert-Einstein-Allee 11, 89081 Ulm, Germany

[3] Institute of Inorganic Chemistry I, Ulm University, Albert-Einstein-Allee 11, 89081 Ulm, Germany

[4] Department of Chemical Sciences, University of Catania, Viale A. Doria 6, 95125 Catania, Italy

[5] Physical Chemistry & Center for Materials Research, Justus Liebig University Giessen, Heinrich-Buff-Ring 17, 35392 Giessen, Germany

[6] Institute for Physical Chemistry (IPC), Friedrich Schiller University Jena, Lessingstraße 10, 07743 Jena Germany

[7] Leibniz Institute of Photonic Technology, Albert-Einstein-Straße 9, D-07745 Jena, Germany

[8] Central Facility of Electron Microscopy, Electron Microscopy Group of Material Science, University of Ulm, Albert-Einstein-Allee 11, 89081 Ulm, Germany

Experimental procedures: Electroless PS-CAT co-deposition using scanning electrochemical cell microscopy (SECCM)

Scanning electrochemical cell microscopy (SECCM)[1,2] is a scanning probe microscopy technique based on the formation of a nanoscale liquid meniscus between the tip of a filled nanopipette and the substrate surface. In contrast to conventional electrochemical cells, the electrolyte is confined within the pipette, and only the small meniscus acts as the reaction microenvironment. When the meniscus touches the surface, it defines a temporary nanoscopic "cell" (typically from 50 nm up to several μm in diameter) in which mass transport, wetting, and solvent evaporation occur within a few seconds[1].
In the present work, a dual-barrel (theta) quartz[3] nanopipette was filled with an acetonitrile solution containing both the photosensitizer (PS) $[Ru(tbbpy)_2(mmip)](PF_6)_3$ (**Ru(mmip)**) and the hydrogen-evolution catalyst (CAT) $[Co(dmgH)_2(py)_2]^+BArF^-$ (**CoBArF**) or **Ru(mmip)** and $[Co(dmgH)_2(py)_2]^+[Co(dmgBPh_2)_2Cl_2]^-$ (**Co^+Co^-**). Each barrel contained a silver quasi-reference counter electrode (QRCE), and a small potential difference (+25 mV) was applied between the two QRCEs. This potential drives a steady ionic current through the electrolyte contained in both barrels and across the liquid meniscus formed at the pipette tip opening. As the pipette approaches the substrate, the meniscus eventually touches the surface, closing the ionic circuit and causing a sudden change in current (**Scheme S1**).

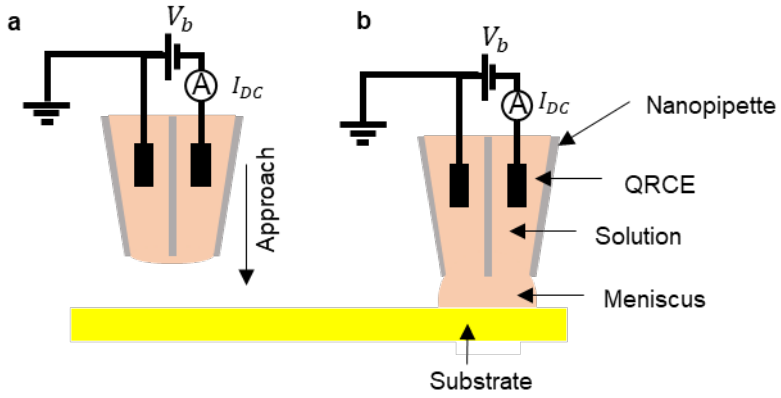

Scheme S1. Schematic illustration of the SECCM meniscus-landing process. **a** A dual-barrel (theta) nanopipette filled with electrolyte solution containing the photosensitizer (PS) and catalyst (CAT) is equipped with Ag quasi-reference counter electrodes (QRCEs) in each barrel. A small potential bias (V_b) applied between the QRCEs drives an ionic current through the electrolyte. **b** As the pipette approaches the substrate, the liquid meniscus at the tip eventually makes contact with the surface, completing the ionic circuit and causing a detectable change in the current. This signal serves as a precise feedback trigger that defines the moment of surface contact, allowing nanometer-controlled positioning of the meniscus for localized, electroless co-deposition of the PS–CAT mixture.

This change serves as a highly sensitive feedback signal that precisely indicates meniscus landing and surface contact, ensuring that the tip stops within nanometer accuracy without physically touching the substrate. Once contact is established, the confined droplet bridges the two QRCEs and the substrate, and co-deposition proceeds without applying an external potential between the tip and the substrate, hence the process is "electroless" rather than electrochemically driven. Under these conditions, the solvent evaporation within the (nano)meniscus concentrates the solutes, driving self-assembly and precipitation of the PS–CAT complex on the substrate. The structure and morphology of the deposit are governed by (i) the local concentration ratio of PS:CAT in the confined volume, (ii) the withdrawal speed of the meniscus/nanopipette, and (iii) the nanopipette orifice diameter. Nanospots are obtained by maintaining the meniscus in contact with the surface for several seconds (5 s) before retraction, allowing isotropic evaporation and nucleation. Nanowires form when the pipette is retracted while the meniscus remains pinned to the surface (withdrawal rate ≈ 150 μm s^{-1}). In this case, solvent evaporation occurs simultaneously with directional meniscus elongation, resulting in one-dimensional supramolecular growth guided by the confined geometry. This (nano)meniscus-guided self-assembly distinguishes SECCM from pressure-driven or ink-based deposition methods such as direct ink writing: SECCM relies on capillary confinement and controlled solvent evaporation rather than viscous flow. The localized deposition volume (femtoliters) and real-time ionic-current feedback provide sub-100 nm spatial precision and reproducible nanostructure formation.

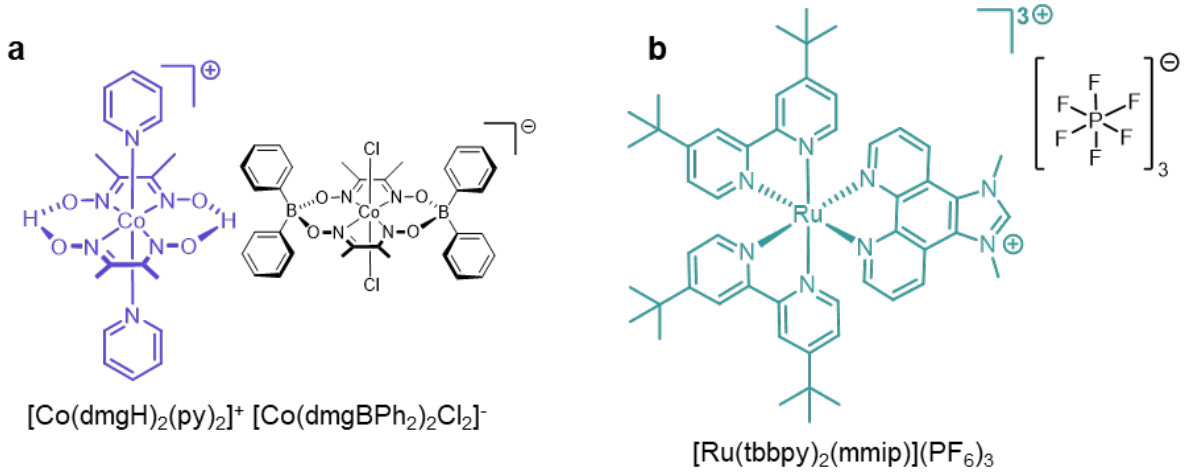

Fig. S1 | Chemical structure of **a** the **$Co^{+}Co^{-}$** catalyst and **b** the **Ru(mmip)** photosensitizer.

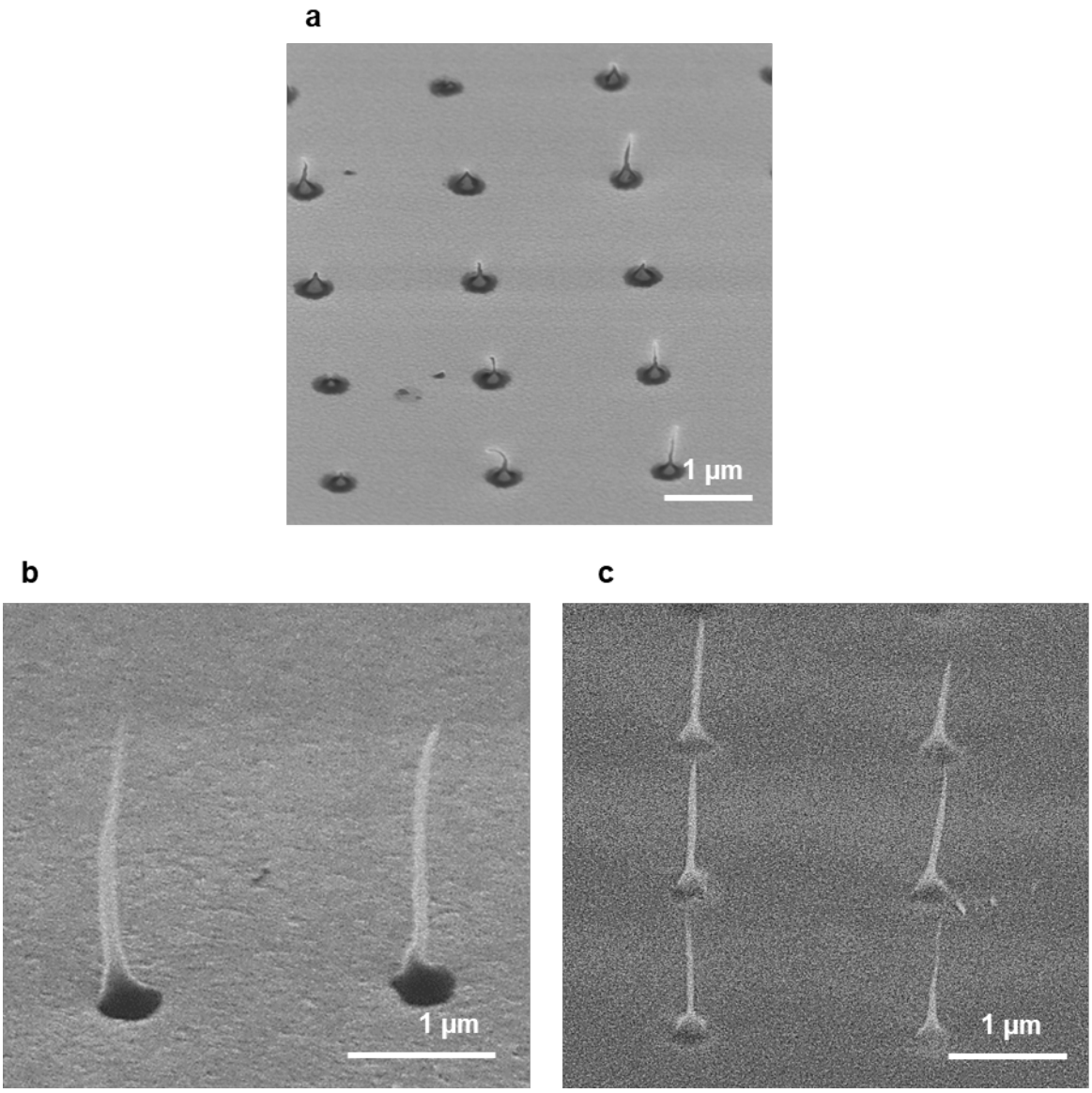

Fig. S2 | a SEM images of $[Ru(bpy)_3](PF_6)_2$/**CoBArF** nanowires deposited on gold. **b-c** SEM images of **Ru(mmip)**/**CoBArF** nanowires deposited on **c** ITO, and **d** HOPG.

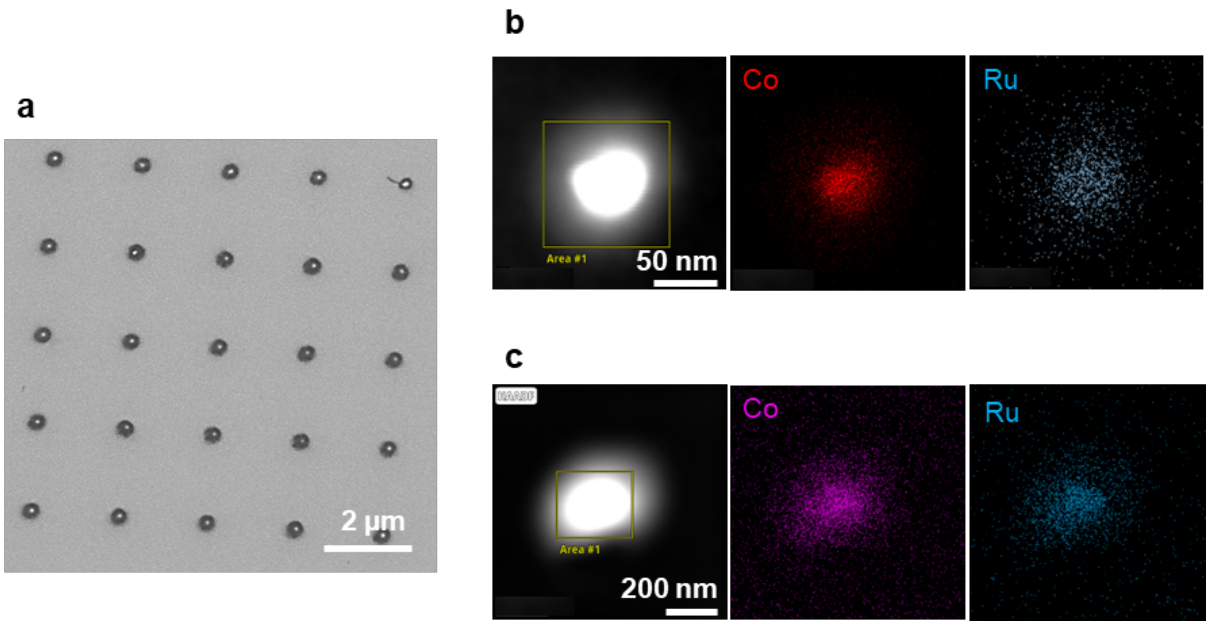

Fig. S3 | **a** SEM images of **Ru(mmip)/CoBArF** nanospots with PS:CAT ratio of 3:1 **b**-**c** HAADF-STEM images and corresponding color-coded EDX elemental maps for the Co, and Ru distribution of **Ru(mmip)/CoBArF** nanospots with PS:CAT ratio of **a** 1:1 and **b** 3:1.

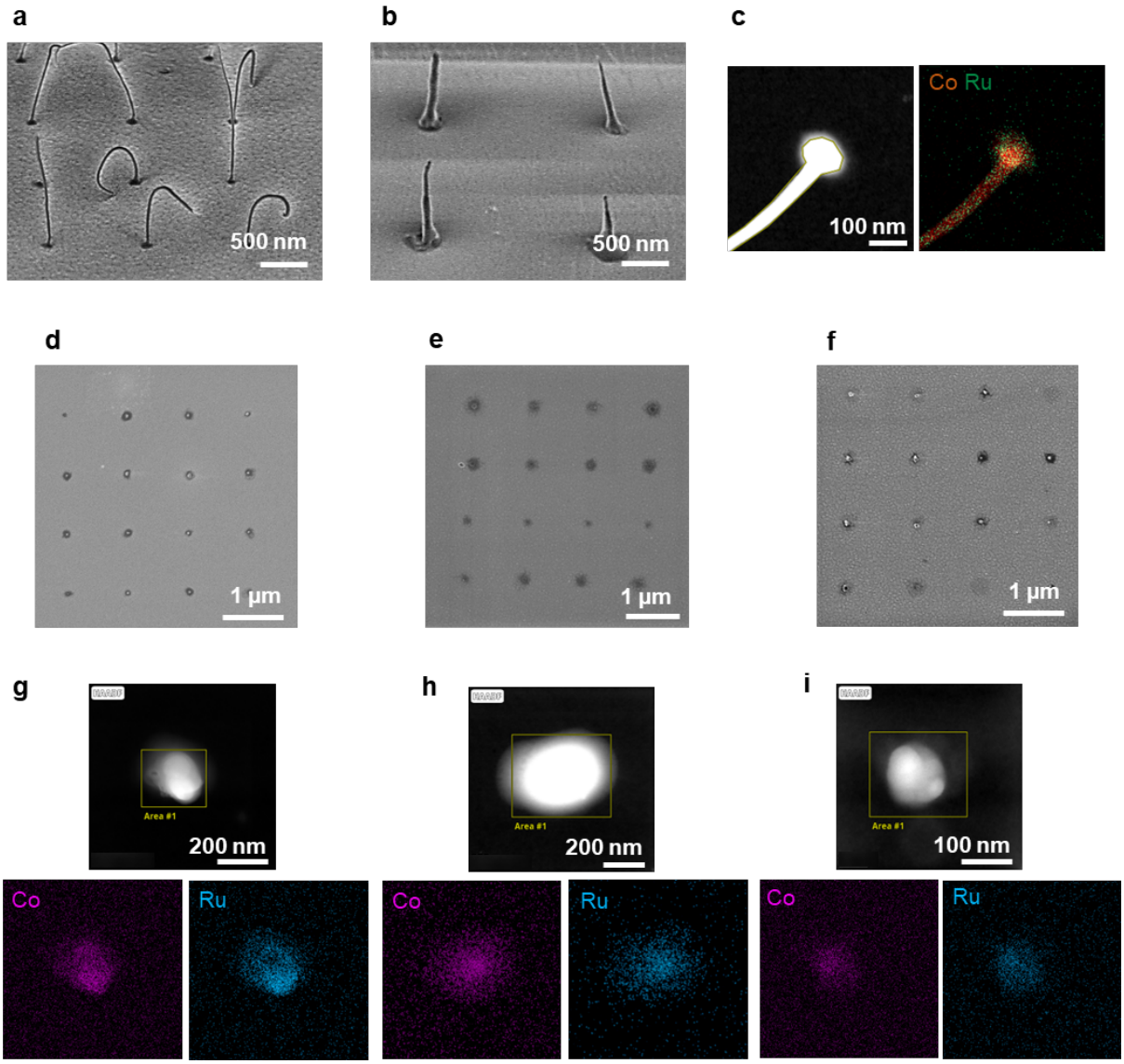

Fig. S4 | **a**-**b** SEM images of **Ru(mmip)/Co^{+}Co^{-}** nanowires with PS:CAT ratio of **a** 1:1 and **b** 3:1. **c** HAADF-STEM image and corresponding color-coded EDX elemental map for the Co, and Ru distribution of the **Ru(mmip)/Co^{+}Co^{-}** nanowire with PS:CAT ratio of 1:1. **d**-**f** SEM images of **Ru(mmip)/Co^{+}Co^{-}** nanowires with PS:CAT ratio of **d** 1:1 and **e** 3:1, and **f** 5:1. **g**-**i** HAADF-STEM images and corresponding color-coded EDX elemental maps for Co, and Ru distribution of **Ru(mmip)/Co^{+}Co^{-}** nanospots with PS:CAT ratio of **g** 1:1, **h** 3:1, and **i** 5:1.

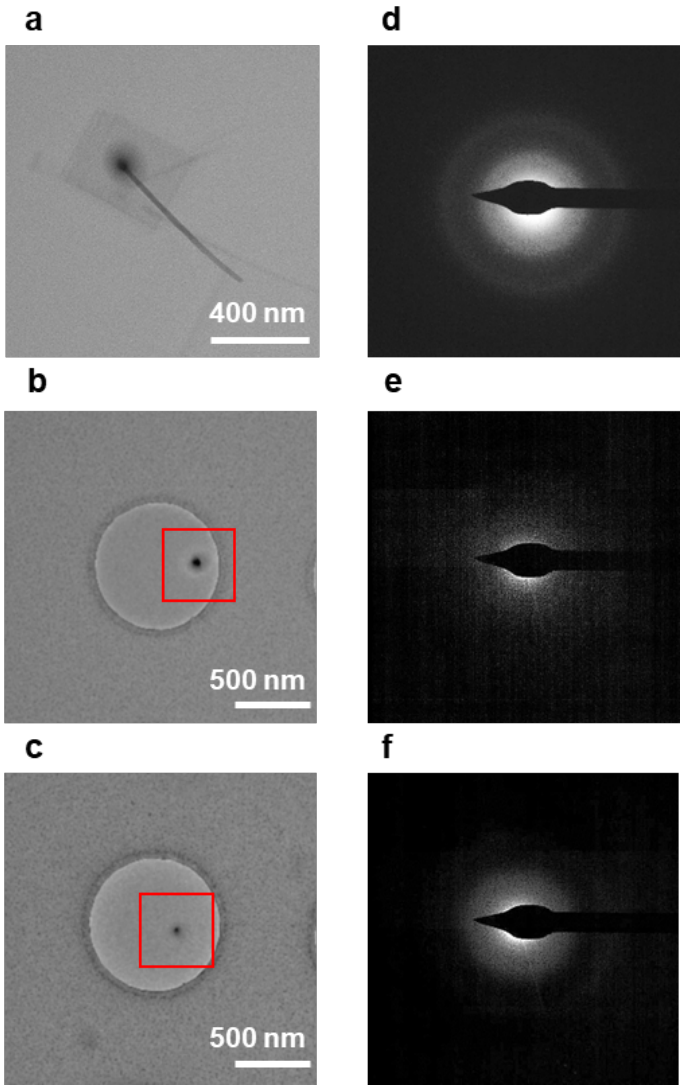

Fig. S5 | **a**-**c** Bright-Field TEM images of **a** a **Ru(mmip)**/**CoBArF** nanowire; **b** a **Ru(mmip)**/**CoBArF** nanowire, and **c** a **Ru(mmip)**/**$Co^{+}Co^{-}$** nanospot (all deposited on a CVD graphene covered holey TEM carbon grid). **d**-**f** Selected area electron diffraction (SAED) patterns of **d** the **Ru(mmip)**/**CoBArF** nanowire, **e** the **Ru(mmip)**/**CoBArF** nanospot and **f** the **Ru(mmip)**/**$Co^{+}Co^{-}$** nanospot. PS:CAT ratio of the nanostructure is 3:1.

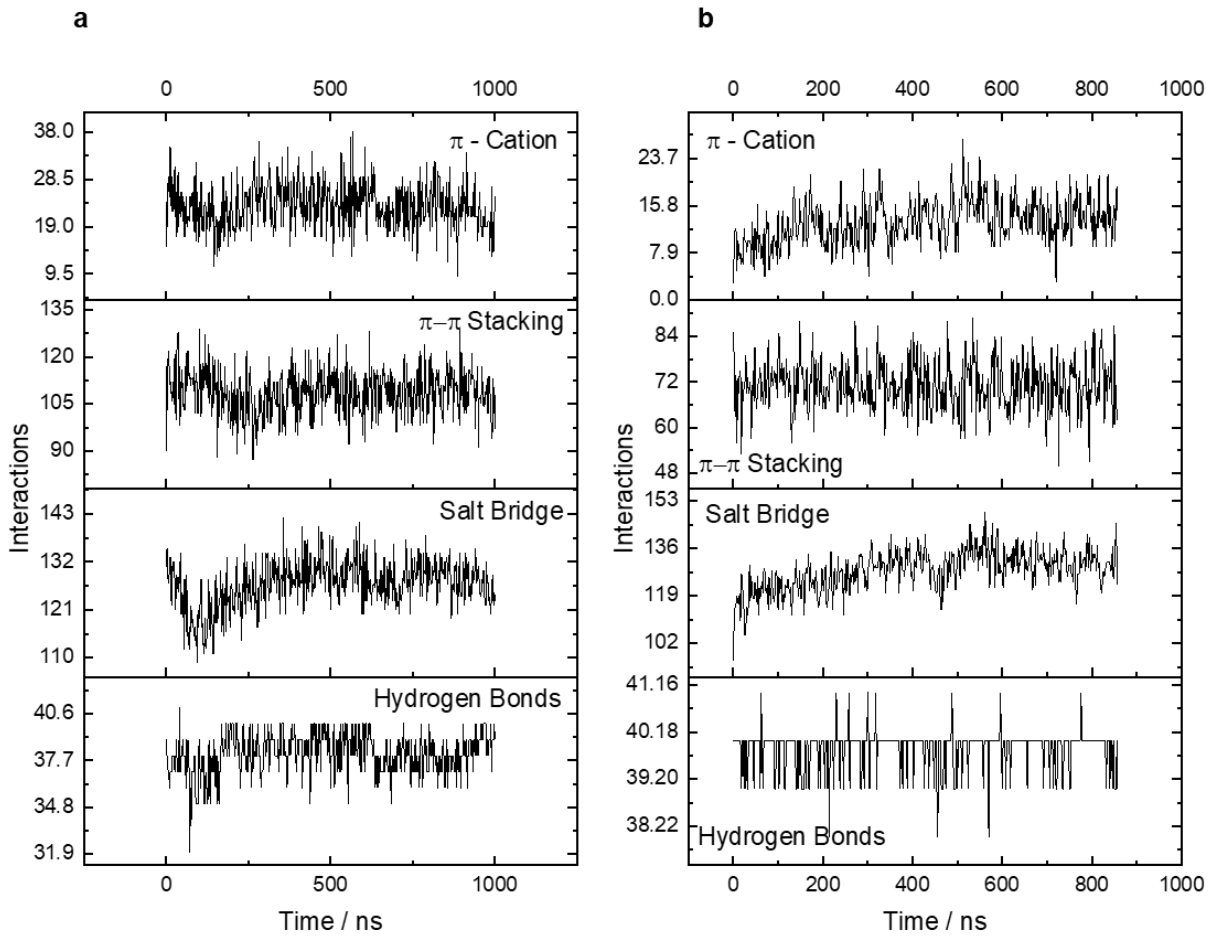

Fig. S6 | Non-covalent interaction mapping for the PS:CAT (ratio of 3:1) system in presence (a) and absence (b) of acetonitrile, depicting differences in salt bridges, hydrogen bonds, π–cation, and π–π interactions.

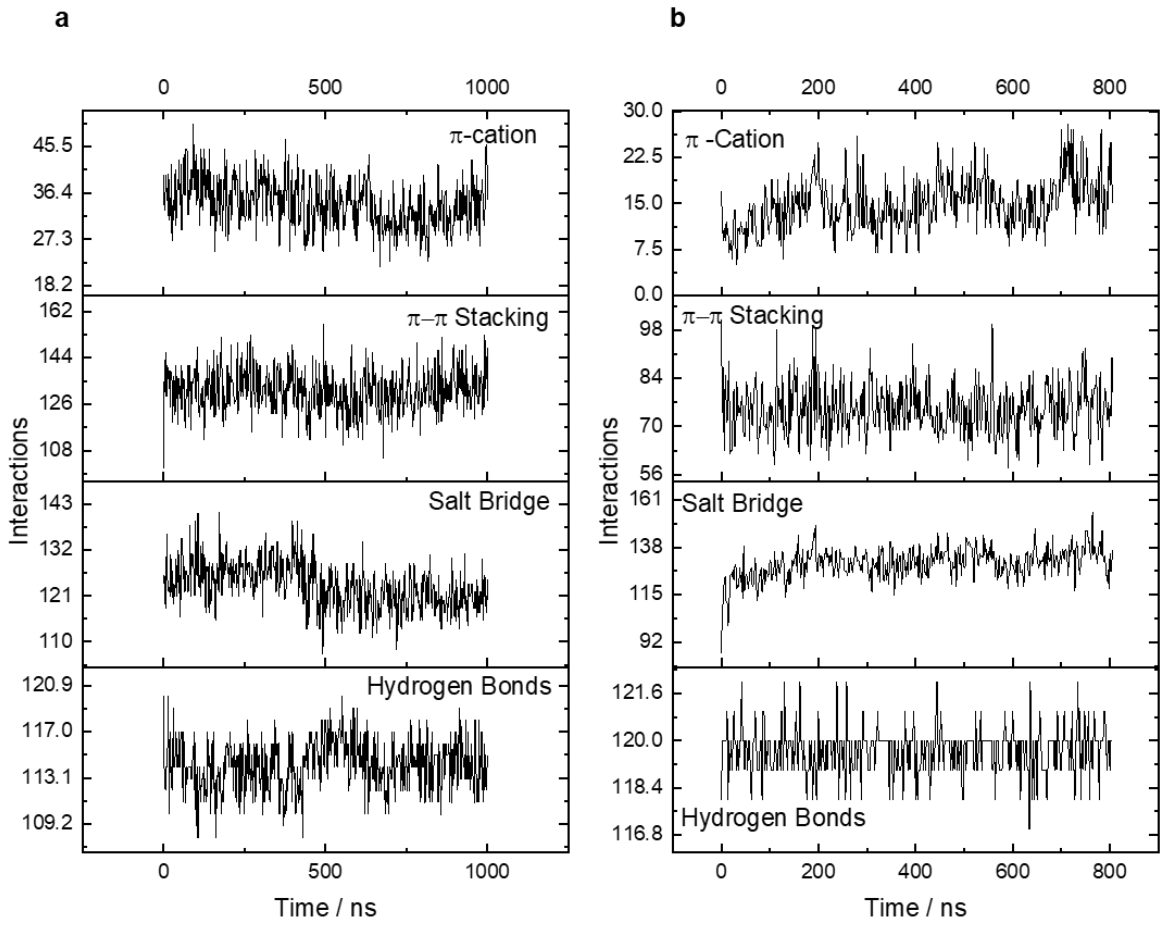

Fig. S7 | Non-covalent interaction mapping for the PS:CAT (ratio of 1:1) system in presence (a) and absence (b) of acetonitrile, depicting differences in salt bridges, hydrogen bonds, π–cation, and π–π interactions.

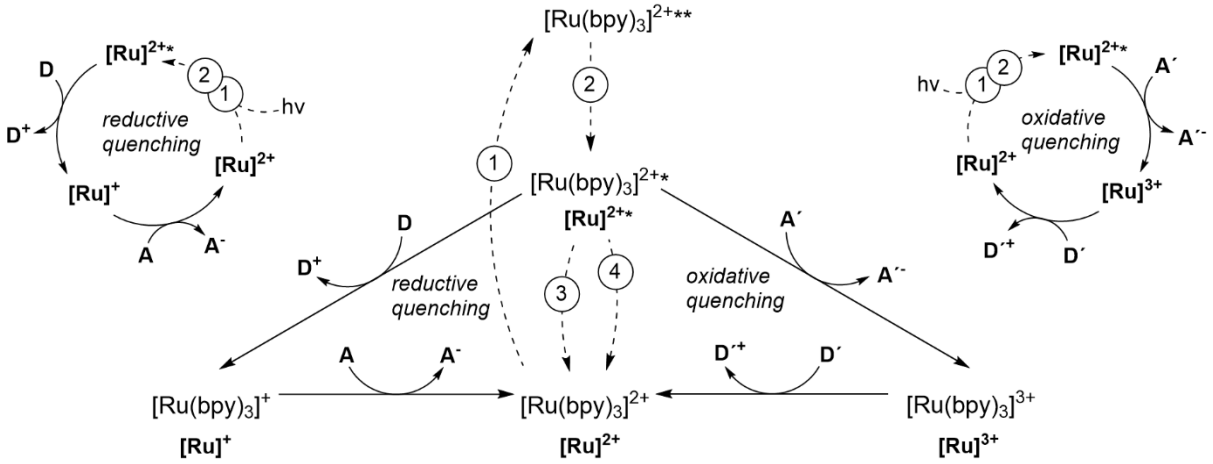

Fig. S8| Generic photoredox cycles for Ru(II)polypyridyl photosensitizers using $[Ru(bpy)_3]^{2+}$ as example. Upon photoexcitation (①), $[Ru(bpy)_3]^{2+}$ is promoted to its metal-to-ligand charge-transfer (MLCT) excited state $[Ru(III)(bpy^{\cdot-})(bpy)_2]^{2+*}$ in singlet multiplicity from which it relaxes (②) to the lowest ^{3}MLCT state. From this ^{3}MLCT state either radiative or non-radiative relaxation may occur (③,④). In the presence of reaction partners with suitable redox potentials, two competing quenching pathways are possible: (left) reductive quenching, in which an electron donor (D) reduces the excited photosensitizer to the reduced species $[Ru(II)(bpy^{\cdot-})(bpy)_2]^{+}$ ($[Ru]^{+}$); and (right) oxidative quenching, in which an electron acceptor (A´) oxidizes the excited state to $[Ru(III)(bpy)_3]^{3+}$ ($[Ru]^{3+}$). In photocatalytic systems, both routes can ultimately regenerate the ground-state $[Ru(bpy)_3]^{2+}$. The feasibility and relative rates of both processes strongly depend on the redox potentials of D/D^+ and $A´^{-}/A´$. In the present contribution, the A or A´ is represented by the utilized cobalt catalysts and donors D or D´ are represented by ascorbic acid and triethanolamine, respectively.

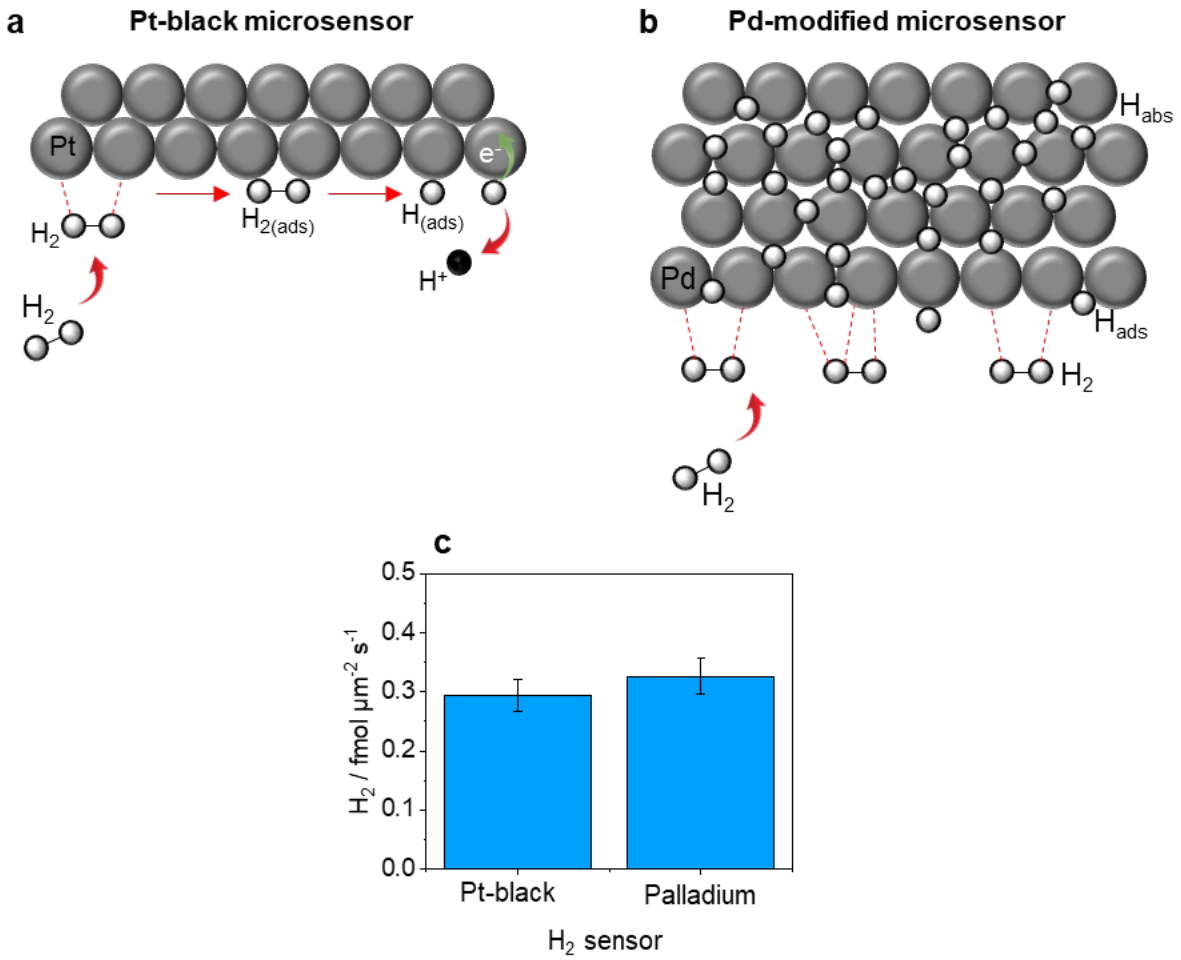

Fig. S9 | **a**-**b** Schematic representation of the mechanism of H_2 detection using **a** Pt-black-modified microelectrode and **b** a Pd-modified (**b**) microsensor. **c** Comparison of the H_2 evolution reaction rate obtained at **Ru(mmip)**/**CoBArF** nanowires (PS:CAT ratio of 3:1) using Pt-black- and Pd-modified microsensors (measurements in 0.1 ascorbic acid (AA, pH = 4) solution. Illumination performed at λ = 470 nm. All error bars reflect the measurement of three different samples.

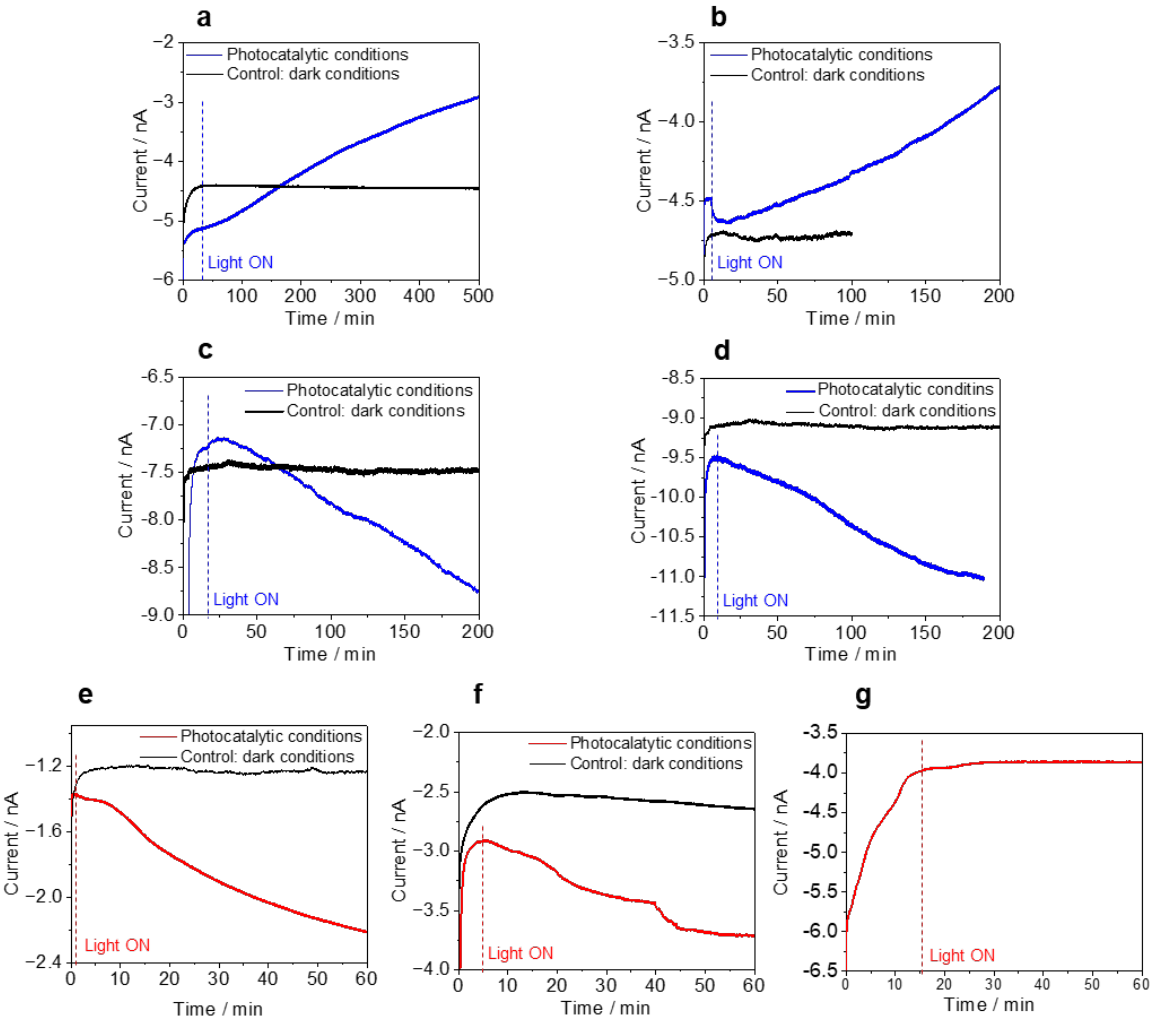

Fig. S10 | **a**,**b** Exemplary chronoamperometric curves recorded using Pt-black H_2 sensor positioned ca. 20 µm above 9 x 9 arrays of **a Ru(mmip)/CoBArF** nanowires (PS:CAT ratio 3:1) immersed in an 0.1 M AA solution and **b Ru(mmip)/CoBArF** nanowires (PS:CAT ratio 3:1) immersed in triethanolamine serving as electron donor. Applied potential: -0.05 V vs. Ag/AgCl to trigger the adsorption-oxidation of H_2 (anodic current recorded). **c**-**d** Exemplary chronoamperometric curves recorded using the Pd-modified H_2 sensor positioned ca. 20 µm above 9 x 9 arrays of **c Ru(mmip)/CoBArF** (PS:CAT ratio 3:1) nanowires and **d** nanospots immersed in an 0.1 M AA solution. Applied potential: -0.60 V vs. Ag/AgCl to trigger the absorption of H_2 (cathodic current recorded). **e**-**g** Exemplary chronoamperometric curves recorded using the Pd-modified H_2 sensor positioned ca. 20 µm above 9 x 9 arrays of **Ru(mmip)/$Co^{+}Co^{-}$** nanospots with PS:CAT ratio equal to **e** 1:1, **f** 3:1, and **g** 5:1. Applied potential: -0.60 V vs. Ag/AgCl to trigger the absorption of H_2 (cathodic current recorded). Black curves correspond to control experiments performed in dark conditions. Illumination performed at λ = 470 nm.

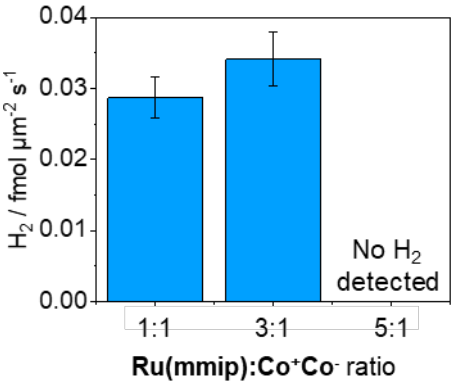

Fig. S11 | H_2 evolution reaction rate obtained at **Ru(mmip)**/**Co$^+$Co$^-$** nanospots at PS:CAT ratio equal to 1:1, 3:1, and 5:1 after one hour of illumination in presence of 0.1 M AA solution serving as sacrificial electron donor. Illumination performed at λ = 470 nm. All error bars reflect the measurement of three different samples.

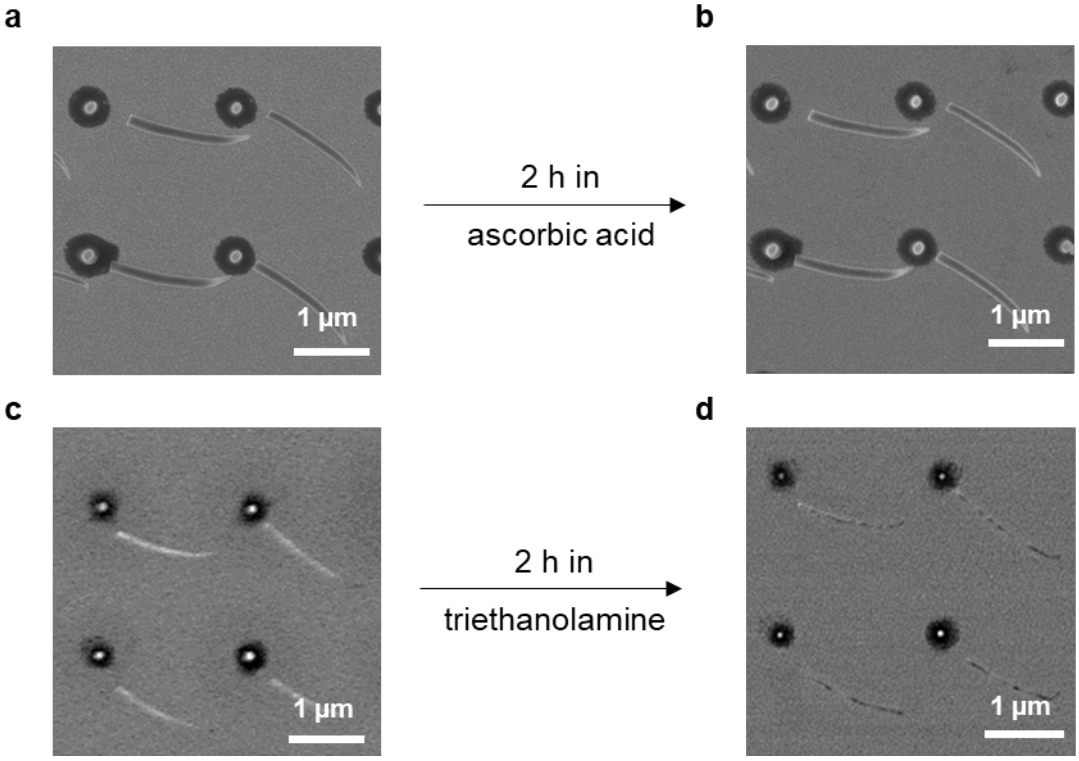

Fig. S12 | **a**-**b** SEM images of **Ru(mmip)**/**CoBArF** nanowires **a** before and **b** after two hours of immersion in an 0.1 M AA solution under photocatalytic conditions (λ = 470 nm). **c**-**d** SEM images of **Ru(mmip)**/**CoBArF** nanowires **c** before and **d** after two hours of immersion in triethanolamine (TEOA, pH =10.3) solution under photocatalytic conditions (λ = 470 nm). The presence of triethanolamine clearly shows the degradation of the nanowires over time.

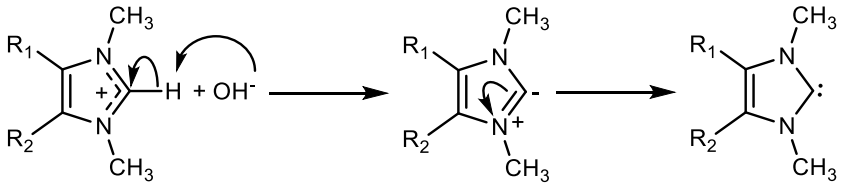

Scheme S2 | Degradation/deprotonation pathway of imidazolium cations in alkaline media following the formation of a carbene.

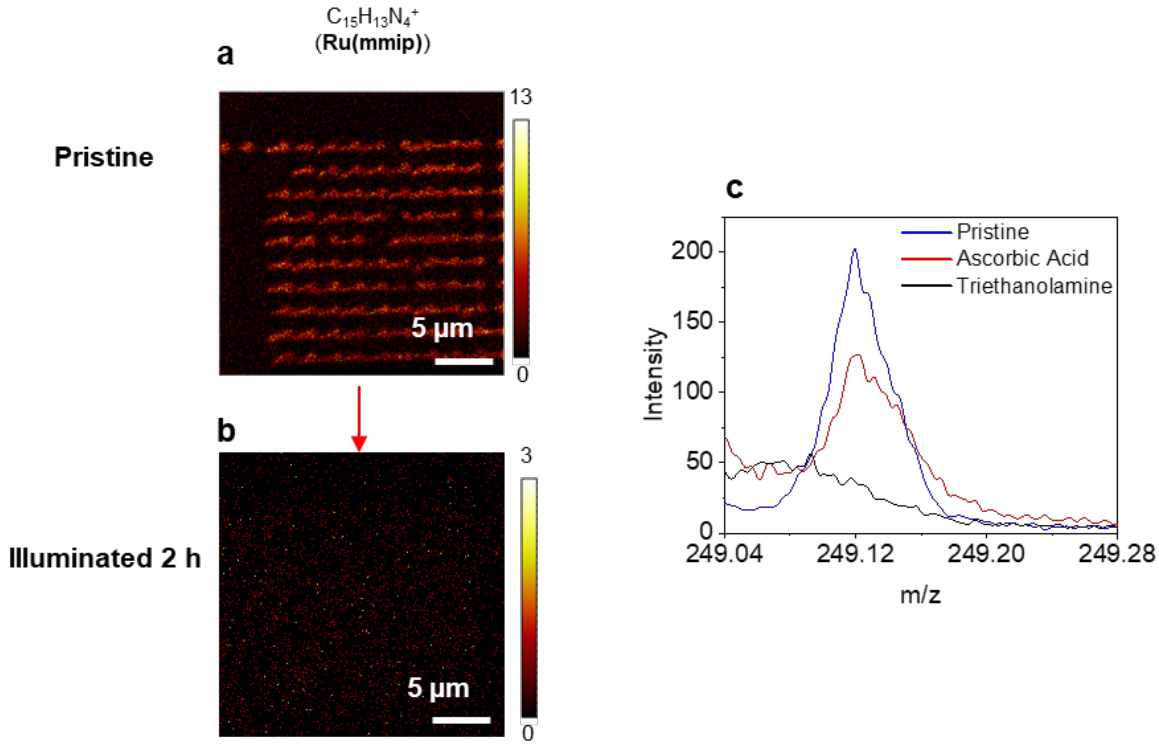

Fig. S13| **a-b** Positive ion mode images of nanowire arrays **a** before and **b** after 2 h of illumination in TEOA solution. The major fragment detected corresponds the basal ligand with the imidazolium functional group. **c** ToF-SIMS positive-ion mass spectra of the m/z 249.1 peak envelope of the nanowire samples before (blue line) and after 2 h of illumination in an 0.1 M AA solution (red line) and TEOA solution (black line).

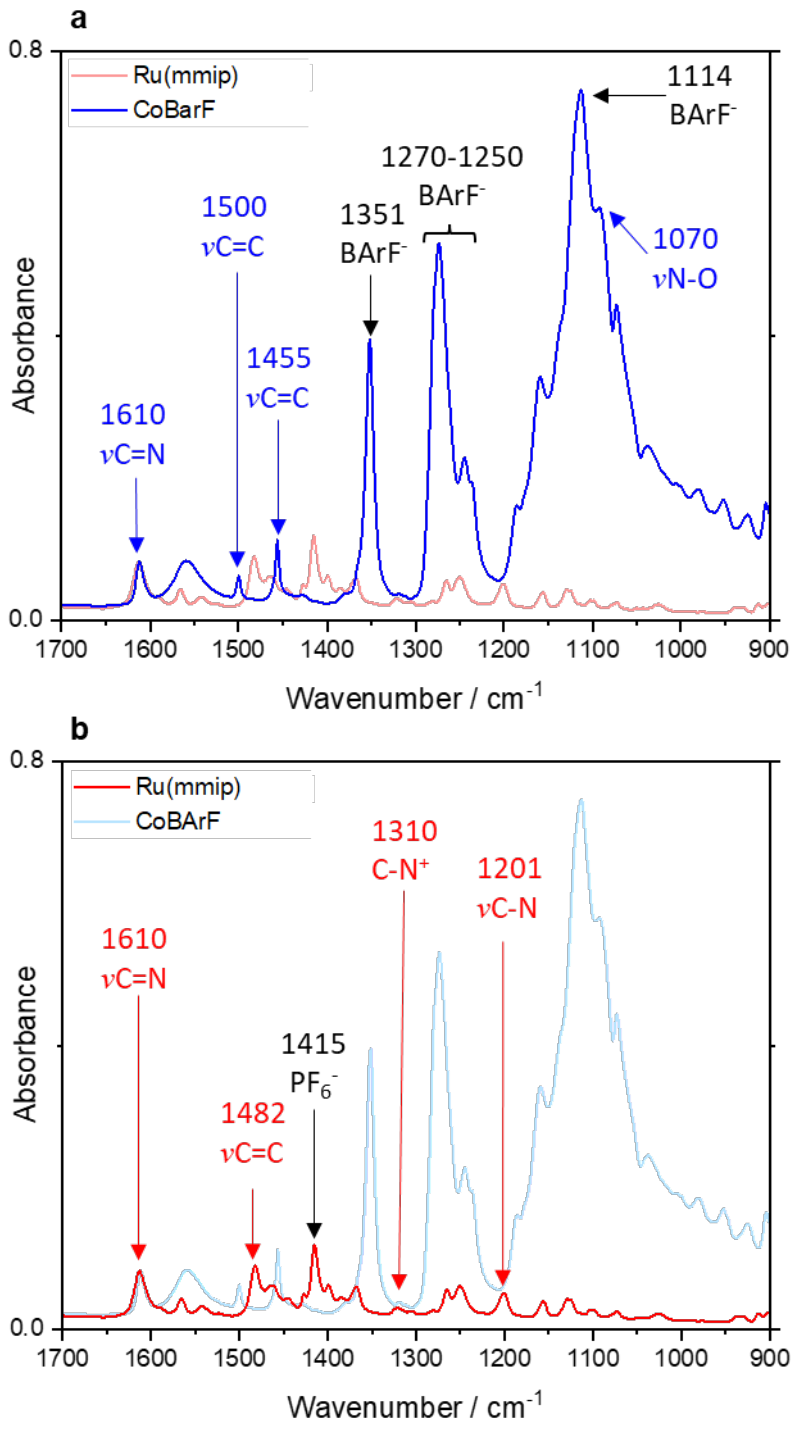

Fig. S14 | **a-b** FT-IR spectra of the **Ru(mmip)** (**a**) and **CoBArF** (**b**) powders used as reference for the Nano-IR measurements of the nanostructures. Peaks highlighted in blue indicate vibrations attributed to the cobaloxime catalyst (CAT), those in red to the **Ru(mmip)** photosensitizer (PS), and those in black to the non-active counterions ($BArF^-$ and PF_6^-).

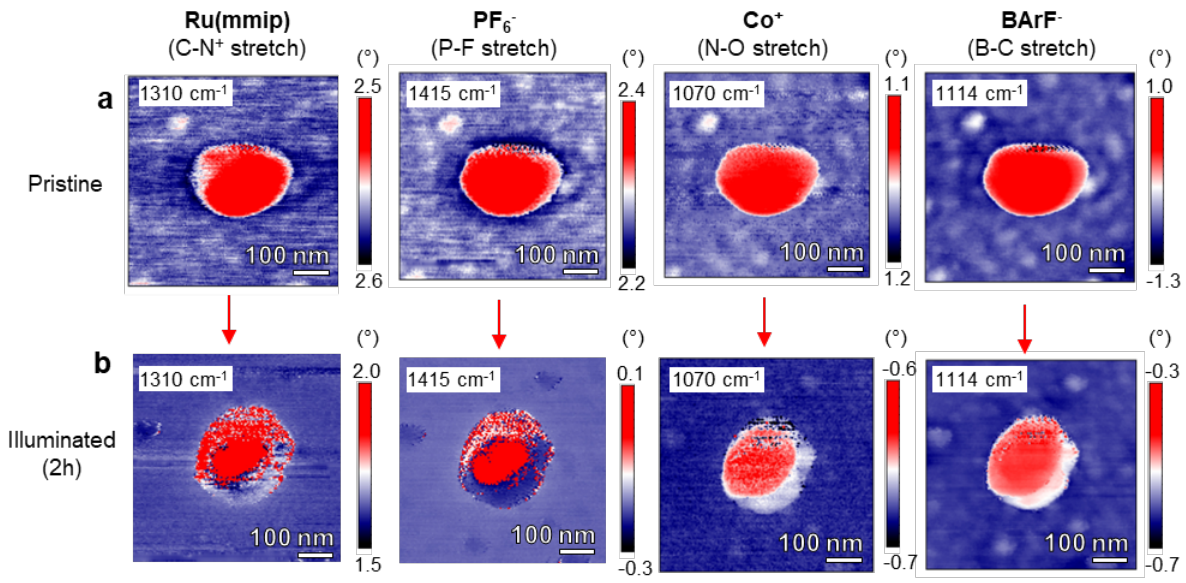

Fig. S15 | Nano-IR images **a** before and **b** after one hour of illumination excited at 1310, 1415, 1070 and 1114 cm^{-1} to target the presence of the **Ru(mmip)** complex, the PF_6^- counterion, the cobaloxime compound and the $BArF^-$ counterion, respectively. Scales correspond to the absorbance detected.

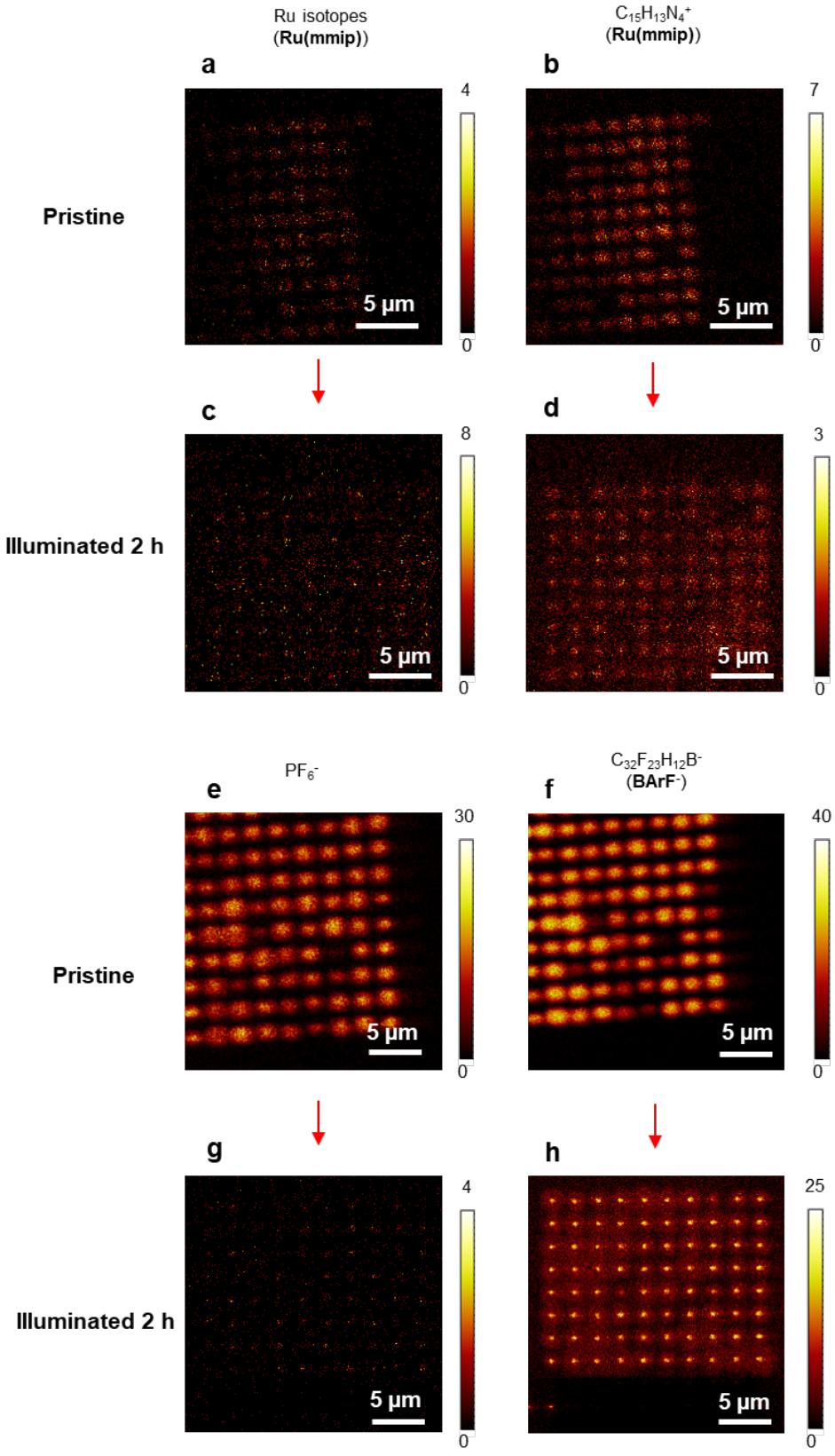

Fig. S16 | a-d Positive ion mode images of nanowire arrays **a,b** before and **c,d** after 2 h of illumination in 0.1 M AA solution. The major fragments detected corresponds to **a**,**c** the Ru isotopes (sum $^{98}Ru^+$, $^{99}Ru^+$, $^{100}Ru^+$, $^{101}Ru^+$, $^{102}Ru^+$) and **b**,**d** the basal ligand with the imidazolium functional group. **e-h** Negative ion mode images of nanowire arrays **e**,**f** before and **g**,**h** after 2 h of illumination. The major fragments detected correspond to **e-g** the PF_6^- counterion and **f**,**h** the BArF$^-$ counterion.

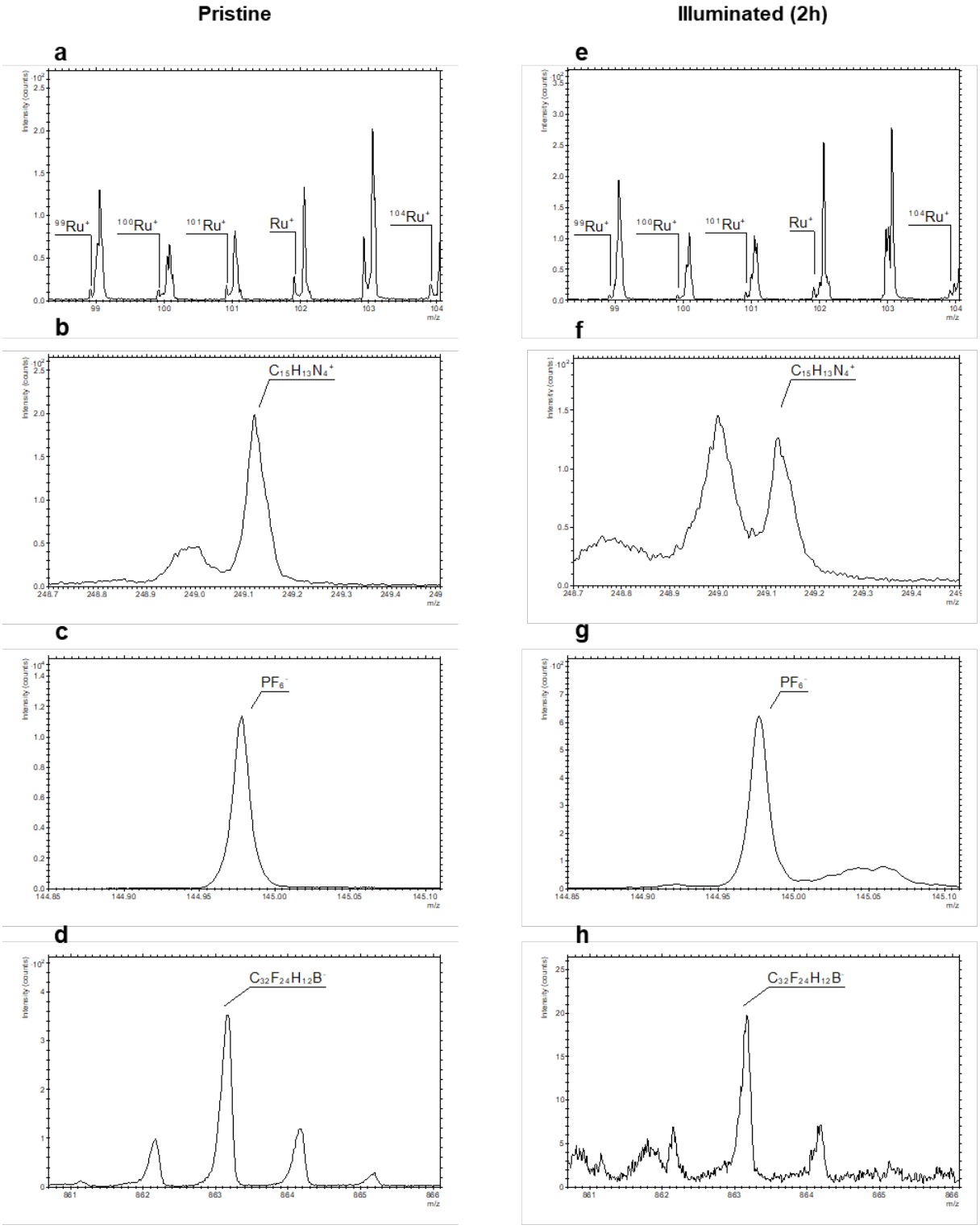

Fig. S17 | Zoomed MS spectra of the Ru signal recorded at the nanowires arrays representing **a**,**e** Ru isotopes, **d**,**f** imidazolium fragment, **c**,**g** PF_6^- counterion, and **d**,**h** $BArF^-$ counterion, **a**-**d** before and **e**-**h** after illumination.

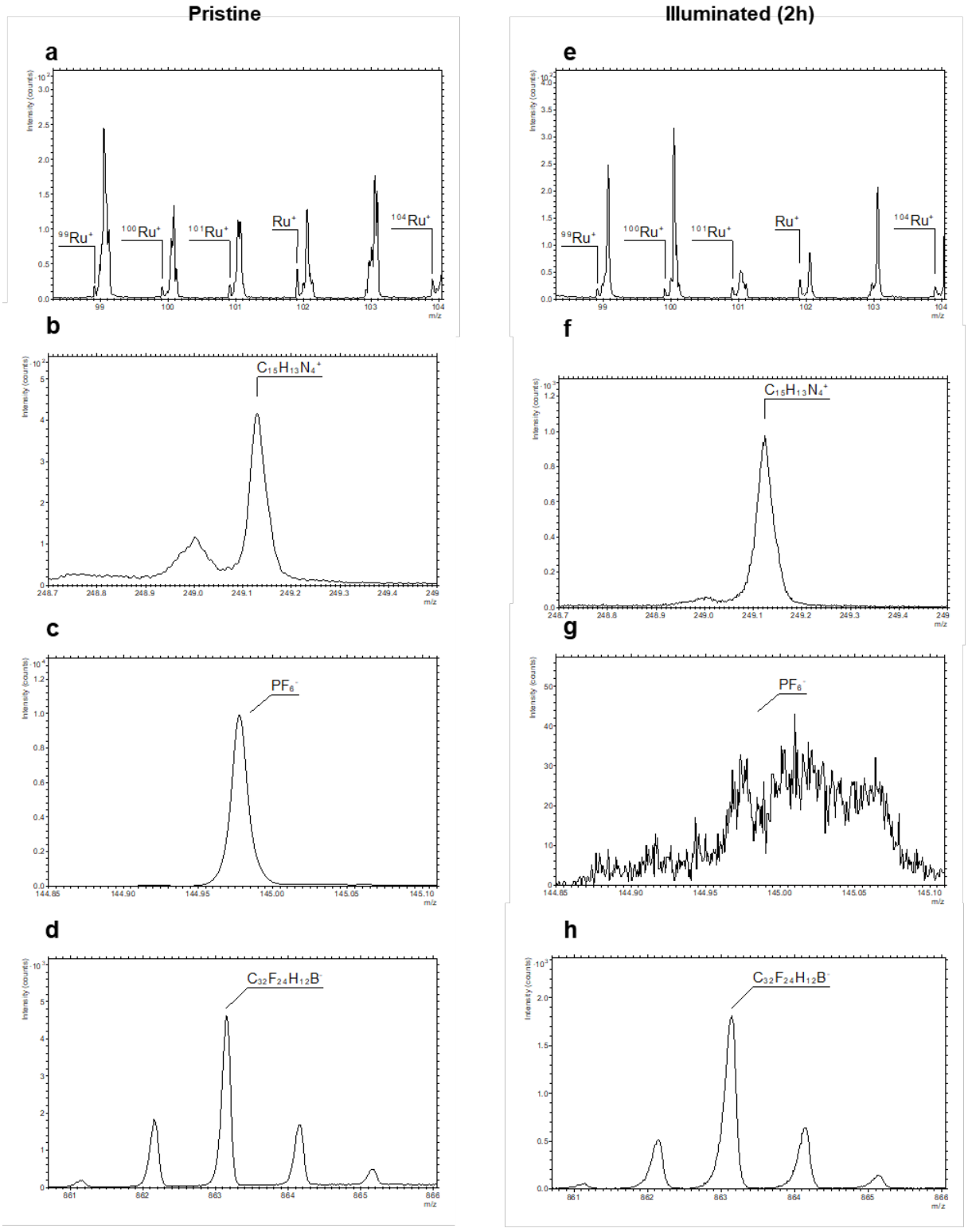

Fig. S18 | MS zoomed spectra recorded at the nanospots arrays representing **a**,**e** Ru isotopes, **d**,**f** imidazolium fragment, **c**,**g** PF_6^- counterion, and **d**,**h** $BArF^-$ counterion, **a**-**d** before and **e**-**h** after illumination.

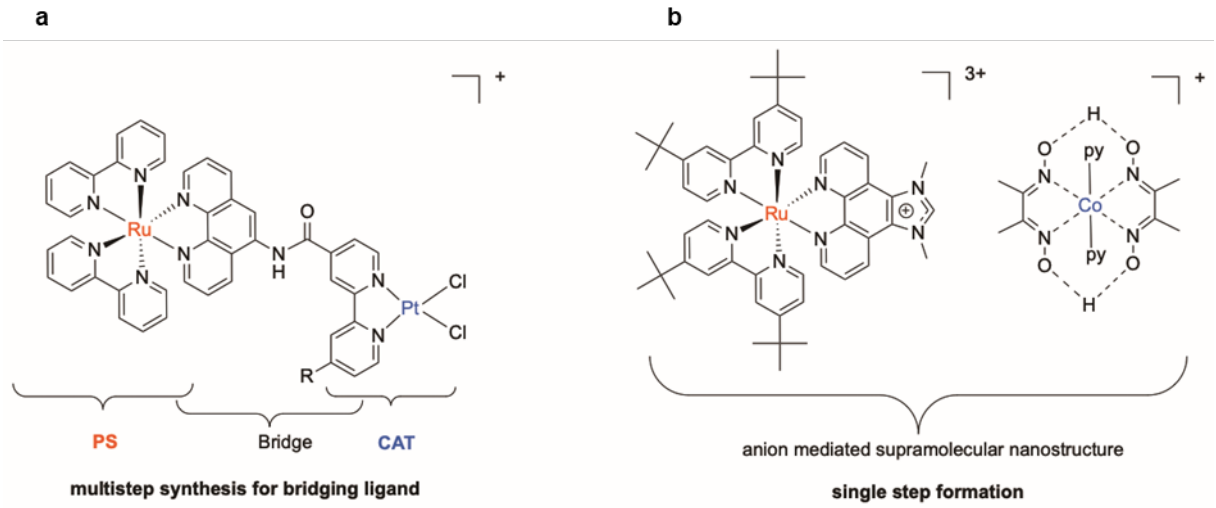

Fig. S19| a Dyadic photocatalyst consisting of PS, BL and CAT; here synthesis of BL requires advanced synthesis tools, time and resources; **b** supramolecular nanostructure architecture consisting of PS and CAT without synthetically challenging BL[4].

References

[1] C.L. Bentley, M. Kang, P.R. Unwin, Scanning electrochemical cell microscopy: New perspectives on electrode processes in action, Curr Opin Electrochem. 6 (2017) 23–30. https://doi.org/10.1016/j.coelec.2017.06.011.

[2] N. Ebejer, A.G. Güell, S.C.S. Lai, K. McKelvey, M.E. Snowden, P.R. Unwin, Scanning Electrochemical Cell Microscopy: A Versatile Technique for Nanoscale Electrochemistry and Functional Imaging, Annu Rev Anal Chem. 6 (2013) 329–351. https://doi.org/10.1146/annurev-anchem-062012-092650.

[3] L.C. Yule, V. Shkirskiy, J. Aarons, G. West, C.L. Bentley, B.A. Shollock, P.R. Unwin, Nanoscale Active Sites for the Hydrogen Evolution Reaction on Low Carbon Steel, J Phys Chem C. 123 (2019) 24146–24155. https://doi.org/10.1021/acs.jpcc.9b07216.

[4] H., Ozawa, M., Haga, K., Sakai, A Photo-Hydrogen-Evolving Molecular Device Driving Visible-Light-Induced EDTA-Reduction of Water into Molecular Hydrogen. Journal of the American Chemical Society, 128 (2006), 4926–4927. https://doi.org/10.1021/ja058087h